Published in final edited form as:
J Bone Miner Metab. 2012 March ; 30(2): 243–251. doi:10.1007/s00774-011-0333-1.

In vivo estimation of bone stiffness at the distal femur and proximal tibia using ultra-high-field 7-Tesla magnetic resonance imaging and micro-finite element analysis

Gregory Chang,
Quantitative Multinuclear Musculoskeletal Imaging Group, Center for Biomedical Imaging, Department of Radiology, NYU Langone Medical Center, 660 First Avenue, Room 231, New York, NY 10016, USA, gregory.chang@nyumc.org

Chamith S. Rajapakse,
Laboratory for Structural NMR Imaging, Department of Radiology, Hospital of the University of Pennsylvania, 3400 Spruce Street, Philadelphia, PA 19104, USA

James S. Babb,
Center for Biomedical Imaging, Department of Radiology, NYU Langone Medical Center, 660 First Avenue, 4th floor, New York, NY 10016, USA

Stephen P. Honig,
Osteoporosis Center, Hospital for Joint Diseases, 301 East 17th Street, Suite 1101, New York, NY 10003, USA

Michael P. Recht, and
Department of Radiology, NYU Langone Medical Center, 660 First Avenue, 4th floor, New York, NY 10016, USA

Ravinder R. Regatte
Quantitative Multinuclear Musculoskeletal Imaging Group, Center for Biomedical Imaging, Department of Radiology, NYU Langone Medical Center, 660 First Avenue, Room 231, New York, NY 10016, USA

Abstract

The goal of this study was to demonstrate the feasibility of using 7-Tesla (7T) magnetic resonance imaging (MRI) and micro-finite element analysis (μFEA) to evaluate mechanical and structural properties of whole, cortical, and trabecular bone at the distal femur and proximal tibia in vivo. 14 healthy subjects were recruited (age 40.7 ± 15.7 years). The right knee was scanned on a 7T MRI scanner using a 28 channel-receive knee coil and a three-dimensional fast low-angle shot sequence (TR/TE 20 ms/5.02 ms, 0.234 mm × 0.234 mm × 1 mm, 80 axial images, 7 min 9 s). Bone was analyzed at the distal femoral metaphysis, femoral condyles, and tibial plateau. Whole, cortical, and trabecular bone stiffness was computed using μFEA. Bone volume fraction (BVF), bone areas, and cortical thickness were measured. Trabecular bone stiffness (933.7 ± 433.3 MPa) was greater than cortical bone stiffness (216 ± 152 MPa) at all three locations ($P < 0.05$). Across locations, there were no differences in bone stiffness (whole, cortical, or trabecular). Whole, cortical, and trabecular bone stiffness correlated with BVF ($R \geq 0.69$, $P < 0.05$) and inversely correlated with corresponding whole, cortical, and trabecular areas ($R \leq -0.54$, $P < 0.05$), but not

Correspondence to: Gregory Chang.

Conflict of interest None.

with cortical thickness ($R < -0.11$, $P > 0.05$). Whole, cortical, and trabecular stiffness correlated with body mass index ($R \geq 0.62$, $P < 0.05$). In conclusion, at the distal femur and proximal tibia, trabecular bone contributes 66–74% of whole bone stiffness. 7T MRI and μFEA may be used as a method to provide insight into how structural properties of cortical or trabecular bone affect bone mechanical competence in vivo.

Keywords

Bone stiffness; Finite element analysis; Ultra high field; 7 Tesla MRI; Osteoporosis

Introduction

Over the past few decades, there has been increasing interest in both the clinical and research communities to identify novel imaging biomarkers of bone strength and quality [1, 2]. Although bone mineral density (BMD) as measured by dual-energy X-ray absorptiometry (DEXA) is used for the diagnosis of osteoporosis and as a surrogate marker for fracture risk, BMD is inadequate because it accounts for only approximately 60% of the variance in bone strength [3]. Furthermore, because DEXA is a 2-dimensional (2D) planar projection technique, BMD measurements can be rendered inaccurate secondary to calcifications overlying bone (e.g., atherosclerotic arteries, heterotopic bone, osteophytes) or changes in patient positioning [4, 5].

Trabecular bone microarchitecture is known to be an important contributor to bone strength and quality [6]. Over the past 15 years, it has become possible with high-resolution, peripheral quantitative computed tomography (HRpQCT) [7, 8] and high-resolution magnetic resonance imaging (MRI) to obtain images of bone microarchitecture in vivo [9, 10]. Because of ionizing radiation dose exposure limits in computed tomography (CT) and signal-to-noise ratio limits in MRI, such imaging is restricted to evaluation of the distal extremities (distal radius, distal tibia) and cannot currently be performed in the hip or spine, two clinically important sites of fracture. Nevertheless, interest in these high-resolution imaging techniques persists because (1) they avoid the need for bone biopsy in patients to obtain micro-architectural information, and (2) the information obtained can still serve as a marker of bone quality in the hip and spine, since osteoporosis is a systemic disease [11–13].

Over the past decade, MRI has benefited from the arrival of high-field (HF) 3 Tesla (3T) and ultra-high-field (UHF) ≥7 Tesla (7T) MRI scanners [14–17]. The advantage of scanning at HF/UHF is greater signal-to-noise ratio (SNR), which scales approximately linearly with the magnitude of the main magnetic field. This increased SNR can be used to (1) improve image quality when scanning challenging areas, such as more proximal anatomic locations (2) increase image spatial resolution, or (3) scan with greater speed [15]. All of these features are beneficial for high-resolution bone MRI examinations which normally require 15–25 min and, as mentioned above, have been restricted to imaging of the distal extremities. Despite the potential advantages offered by UHF, only a handful of publications have described high-resolution MRI of bone at 7T [18–23].

In parallel with the evolution in MRI scanner technology and improvements in image quality, there have also been progressive advances in image analysis methods and researchers' abilities to extract information from images. Beyond evaluation of bone structure and microarchitecture (e.g., cortical thickness, trabecular thickness, trabecular separation), it is also now possible to perform imaged-based assessments of bone mechanical properties (e.g., stiffness) using micro-finite element analysis (μFEA) [24, 25]. The ability to noninvasively estimate bone mechanical properties from images of bone

represents a powerful new means to gain insight into the mechanical implications of bone structural derangements in osteoporosis or other skeletal disorders (osteoarthritis, osteopetrosis).

With this as background, the primary goals of this study were (1) to use an UHF 7T MRI scanner to perform in vivo high-resolution imaging of bone microarchitecture at more proximal anatomic locations—the distal femur and proximal tibia—with shorter scan times compared to clinical scanners (~7 min, >11 images/min), and (2) to use μFEA to compute the stiffness of trabecular, cortical, and whole bone at these locations. Since the distal radius and distal tibia are already used as surrogate markers for bone quality in the proximal femur [13] and spine [11, 12], the distal femur and proximal tibia should serve as equally good, if not better bone markers of those locations as well. As secondary goals, we also examined the associations between bone stiffness (whole, cortical, and trabecular) and (1) bone structural properties (cortical thickness; whole, cortical, and trabecular bone volume fraction (BVF); and whole, cortical, and trabecular bone cross-sectional area), and (2) body mass index (BMI).

Materials and methods

Subject recruitment

This study had institutional review board approval and written informed consent was obtained. Fourteen healthy subjects without history of bone disorder, metabolic or endocrinologic disorder, or bone-altering medication use were recruited (10 females, median age 46.5 years, range 21–68 years; 4 males, median age 27 years, range 25–30 years).

MRI scanning

The right knee of each subject was scanned on a 7T whole-body MRI scanner (Siemens, Erlangen, Germany) using a new birdcage transmit-28 channel receive knee coil (Quality Electrodynamics, Mayfield Village, OH, USA). The technical details of engineering this coil have been previously described [26]. In brief, the construction of this coil required a partially shielded birdcage transmit design, and the use of ultra-compact low-noise preamplifiers, which are smaller than the typical miniature preamplifiers used commercially at 1.5T and 3T. For high-resolution bone imaging, a 3D fast low-angle shot sequence was employed similar to prior studies [19, 20, 27] (TR/TE 20 ms/5.2 ms, flip angle 10°, bandwidth 130 Hz/pixel, one signal acquired, matrix 512 × 512, field of view 12 cm, 0.234 mm × 0.234 mm, slice thickness 1 mm, 80 axial images). The image resolution in this study, 0.234 mm × 0.234 mm × 1 mm, is adequate to evaluate bone microarchitecture. Recent work by Kim et al. has shown that bone parameters derived from MR images can be preserved up to a resolution of 0.23 mm [28]. Furthermore, since trabeculae are oriented in the weight-bearing superoinferior direction, relaxation of through-plane resolution to 1 mm should not affect the accuracy of bone microarchitectural measurements [10]. Finally, all images were obtained with parallel imaging with an acceleration factor of 2 to achieve an imaging time of 7 min 9 s.

Image processing and generation of BVF map

All images were corrected for signal intensity inhomogeneity caused by MR coil shading using a local thresholding algorithm as previously described [29]. A musculoskeletal radiologist with dedicated knowledge of knee anatomy oversaw all of the segmentations to ensure accuracy. 10-mm-thick volumes of interest of bone at the level of the distal femoral metaphysis (40 mm from the end of bone), femoral condyles (30 mm from the end of bone), and tibial plateau (20 mm from the end of bone) were chosen for analysis (Fig. 1a). Images were manually segmented at the periosteal and endosteal boundaries of cortical bone to

generate 3 datasets corresponding to whole bone, cortical bone, and trabecular bone regions at the distal femoral metaphysis (Fig. 1b, c), femoral condyles (Fig. 1d, e) and tibial plateau (Fig. 1f, g). For each volume of interest, voxel signal intensities were linearly scaled from 0 to 100 with absolute marrow and absolute bone having minimum and maximum values, respectively [30]. This generated a 3D BVF map, with each voxel within the BVF map representing the fractional occupancy of bone from the original MR image.

Micro-finite element analysis

Micro-finite element analysis in the linear elastic regime was performed to compute axial stiffness of each region as previously described [25, 30–32] by simulating compressive loading along the infero-superior direction [29, 30] (Fig. 1a). Studies performed recently on human cadaveric tibial specimens ex vivo have shown excellent correlation between MR-derived and reference standard high-resolution CT-derived (25 μ resolution) measurements of bone stiffness and bone microarchitecture [30, 32]. In brief, each voxel in the BVF map was converted into a hexahedral finite element with dimensions corresponding to the voxel size. The material properties of bone were chosen as iso-tropic and linearly elastic with Young's modulus (YM) set to be linearly proportional to the BVF value such that YM = 15 GPa × BVF while the Poisson's ratio was set at 0.3 for all elements [33]. Simulated compression was applied along the bone's longitudinal axis by applying a constant displacement (~1% strain) to all finite element nodes in the proximal face of the finite element mesh while keeping those in the distal face constrained. The μFE system was solved to yield a 3D strain map for the whole-bone section [25, 30]. Finally, the axial stiffness was obtained as the quotient of the applied strain on the proximal face and the resulting stress.

Reproducibility study for segmentation of bone

We also conducted a reproducibility study for manual segmentation of images. Cortical and trabecular bone segmentations were repeated 3 times (each 1 week apart) on images of 5 randomly selected subjects. The reproducibility was assessed on a primary segmentation parameter (cross-sectional area) and a derived parameter (stiffness).

Statistical analysis

Statistical analysis was performed using SAS (SAS Institute, Cary, NC, USA). Analysis of variance was utilized to compare trabecular bone stiffness with cortical bone stiffness at the distal femoral metaphysis, femoral condyles, and tibial plateau. Spearman rank correlation coefficients were utilized to characterize correlations between bone stiffness and (1) structural parameters, and (2) BMI. For the reproducibility study, the intraclass correlation coefficient (ICC) and the coefficient of variation (CV) of measurements were computed.

Results

Structural and mechanical parameters

Representative images of the distal femur and proximal tibia are shown in Fig. 1. The mean and standard deviation for each MR measurement at each location are shown in Table 1. In brief, for whole bone, mean stiffness at the distal femoral metaphysis, femoral condyles, and tibial plateau were 1424.9 ± 681.0, 1287.6 ± 702.4, and 1226.7 ± 564.4 MPa, respectively. For cortical bone, mean stiffness in the distal femoral metaphysis, femoral condyles, and tibial plateau were 216.0 ± 152.0, 214.2 ± 182.9, and 174.0 ± 107.3 MPa, respectively. For trabecular bone, mean stiffness in the distal femoral metaphysis, femoral condyles, and tibial plateau were 933.7 ± 433.3, 844.0 ± 454.6, and 901.2 ± 396.7 MPa, respectively. For the

reproducibility study, the results were reproducible with ICC >0.99 and a CV ranging from 0.3% to 4.9% (Table 2).

Comparison of bone stiffness within and between locations

At all three locations, trabecular bone stiffness was approximately three-fold greater than cortical bone stiffness ($P < 0.0001$), with the percentage of whole bone stiffness due to trabecular bone ranging from 66% to 74% (Fig. 2a). In addition, at all three locations, trabecular bone represented a greater proportion of the whole BVF compared to cortical bone ($P < 0.0001$ for all, Fig. 2b), with trabecular bone contributing between 67% and 72% of the whole BVF. Differences in bone stiffness (either whole, cortical, or trabecular) between the three locations were not statistically significant ($P > 0.40$ for all).

Relationships between bone stiffness and bone structure

Whole, cortical, and trabecular bone stiffness correlated with BVF at all three locations ($R = 0.75-0.85$, $P < 0.05$ for all) with the exception of cortical bone at the proximal tibia ($R = 0.29$, $P = 0.31$) (Fig. 3).

Within the proximal tibia, whole bone and trabecular bone stiffness inversely correlated with corresponding whole ($R = -0.54$) and trabecular bone areas ($R = -0.56$) ($P < 0.05$ for both) (Fig. 4). Within the distal femoral metaphysis, cortical bone stiffness inversely correlated with cortical bone area ($R = -0.6$, $P = 0.02$) (Fig. 4). There was no correlation between bone stiffness (whole, cortical, or trabecular) and cortical thickness ($R = -0.12$ to -0.56, $P > 0.05$).

Relationships between bone stiffness and BMI

Whole, cortical, and trabecular bone stiffness positively correlated with BMI at the distal femoral metaphysis and femoral condyles ($R = 0.55-0.67$, $P < 0.05$), but not at the proximal tibia ($P \geq 0.14$) (Fig. 5).

Discussion

We have used UHF 7T MRI combined with μFEA to evaluate mechanical and structural properties of whole, cortical, and trabecular bone at the distal femur and proximal tibia in vivo. This method is reproducible with ICC > 0.99 and a CV ranging from 0.3 to 4.9%. At the distal femur and proximal tibia, cortical bone contributed to only a small proportion (<24%) of whole bone stiffness. To our best knowledge, this is the first paper to describe the separate contributions of trabecular and cortical bone to whole bone stiffness at the distal femur and proximal tibia and the first paper to apply finite element analysis to 7T images of bone obtained at these locations. In the future, this method could be used to gain further insight into the mechanical implications of bone structural derangements in osteoporosis, osteoarthritis, or other bone disorders.

Determination of the contributions of trabecular and cortical bone to whole bone stiffness would be difficult to perform via direct mechanical testing of cadaveric femur or tibial specimens ex vivo. Such a study would require a technically challenging, if not impossible, dissection of the curved cortical bone shell from underlying trabecular bone. Already, in vertebral bodies, which have relatively flat cortical surfaces, this is considered difficult [34, 35]. Furthermore, this study would not be possible to carry out using conventional CT scanners, which are low resolution (~0.5 mm), or HRpQCT scanners, which are limited to imaging of the distal extremities (wrist, ankle). Thus, the combination of high-resolution MRI and finite element analysis represents a powerful tool to evaluate bone mechanical properties in vivo, especially in more proximal locations.

The ability to estimate mechanical properties of bone from images is clinically important because ultimately, a bone's ability to resist fracture is related to its mechanical competence or strength [36]. As a research tool, such measures of bone mechanical competence may help us understand how bones become fragile and fracture. As a clinical tool, such measures may one day improve the ability of doctors to assess fracture risk in subjects with osteoporosis. Furthermore, mechanical measures of bone may provide insight into the role of bone abnormalities in other musculoskeletal disorders such as osteoarthritis, where increased subchondral bone stiffness may predispose individuals to cartilage degeneration [37].

The positive correlation between bone stiffness and BVF is not surprising given that BVF directly reflects bone mass, and bone stiffness should correlate with the amount of bone present. The inverse correlation between bone stiffness and bone area is also not surprising, given that stiffness is the stress (force/area) divided by strain (displacement distance/original structure length). The lack of a correlation between bone stiffness (either, whole, cortical, or trabecular) and cortical thickness is most likely due to location of the analysis at the end of bone, where cortical bone is almost uniformly thin and contributes to only a small proportion of whole bone stiffness. Inclusion of analysis at the femoral diaphysis, where cortex is thick, would most likely reveal a relationship between bone stiffness and cortical thickness. Finally, the correlation between bone stiffness and BMI is consistent with the known detrimental effect of low BMI on bone health [38]. Indeed, because low BMI is such a strong risk factor for future fracture, it was included among the items assessed in the World Health Organization FRAX calculator for estimation of osteoporotic fracture risk [39].

The main benefit of performing UHF MRI is the greater SNR available (SNR scales approximately with the magnitude of the main magnetic field) [15]. This SNR can be converted into increases in spatial resolution or decreases in imaging time. In this study, this increased SNR allowed us to perform high-resolution imaging in a more proximal location, the distal femur/proximal tibia, which as mentioned above cannot be imaged by HRpQCT. Bone imaging in this study was also facilitated by the use of a new 28 channel-receive knee coil, which serves as the antenna for reception of the MR signal. Previous high-resolution bone imaging studies of the knee at 7T have used quadrature coils [19, 20, 27]. The advantage of signal reception via multiple channels is an additional gain in SNR [40–42]. The SNR gain of UHF and the multichannel coil permitted us to obtain analyzable images in 7 min 9 s (11.1 images/min), which is faster than on clinical MR scanners. This shortening of the examination time is useful because it reduces the chance for patient discomfort and motion artifact on images. Over time, 7T scanners are likely to become more widespread and these techniques should be available at more centers around the world.

There are limitations to this study. Firstly, the voxel size of the images is lower than that of HRpQCT studies, which can produce images with voxel sizes of 81 μ. Nevertheless, this should not change our overall results. Because our analysis is based on BVF maps, rather than binarized images, grayscale information, reflecting the amount of bone within a voxel is retained. Furthermore, as mentioned previously, HRpQCT is limited to scanning of the distal extremities, such as the wrist or ankle, while MRI is capable of evaluating more proximal locations, such as around the knee and possibly even the proximal femur [43]. Finally, it should be noted that because of point spread function blurring, the effective spatial resolution of high-resolution MRI may actually be equivalent or slightly better than that of HRpQCT [10, 25]. As a second limitation, our MRI protocol involves the use of a gradient-echo imaging sequence, which has the advantage of low-energy deposition, but the disadvantage of magnetic susceptibility artifact. This can cause artifactual broadening of trabeculae on MR images. However, we did use scanning parameters similar to the few

previous high-resolution MRI studies of bone performed at 7T [19, 27]. Furthermore, a fast spin-echo sequence has recently been modified for successful implementation at 7T (3D fast spin-echo with out-of-slab cancellation) [22, 23]. This is promising since such spin-echo-based sequences are less sensitive to off-resonance effects at the bone-marrow interface and can thus produce even more accurate representations of cortical and trabecular bone microarchitecture for assessment of bone quality. Third, we did not carry out inter-user reproducibility studies, as this is a small study with a novel technique and only one person has been trained in our laboratory to perform the segmentation. As we expand our studies and train others to do the segmentation, it will be important to carry out inter-user reproducibility studies. Fourth, for the FEA, we have assumed uniform material properties for bone. Spatial variation in bone mineral content would alter bone material properties and resultant bone stiffness calculated from FEA. In the future, the addition of BMD data to FEA will make this method even more accurate for computations of bone stiffness. Finally, we have not scanned any subjects with osteoporosis. If this technique is to be applicable to disease, it will be important to conduct clinical studies and demonstrate whether MRI and FE-based measurements of bone stiffness in vivo can be used to assess fracture risk or monitor disease progression/treatment response.

In conclusion, we describe the feasibility of performing UHF 7T MRI and FEA of the distal femur and proximal tibia to evaluate the mechanical and structural properties of bone in vivo. This can be performed in 7 min and allows discrimination of the separate contributions of trabecular and cortical bone to whole bone stiffness. Since trabecular bone appears to provide the majority of bone stiffness at the end of long bones, trabecular bone might represent a better therapeutic target for medications aimed at preventing fractures that occur at the end-of-bones. As a research tool, MRI combined with FEA could be utilized to determine how trabecular and cortical bone structural derangements in osteoporosis differentially contribute to alterations in bone mechanical competence. MRI combined with FEA might also be used to determine how alterations in subchondral bone stiffness contribute to cartilage degeneration (also detectable by MRI), and the pathogenesis of osteoarthritis.

Acknowledgments

The authors acknowledge grant support from the Radiological Society of North America (RSNA RR0806) and the United States National Institutes of Health (K23-AR059748, R01-AR053133, R01-AR056260).

References

1. Griffith JF, Engelke K, Genant HK. Looking beyond bone mineral density: imaging assessment of bone quality. Ann N Y Acad Sci. 2010; 1192:45–56. [PubMed: 20392217]
2. Ito M. Recent progress in bone imaging for osteoporosis research. J Bone Miner Metab. 2011; 29:131–140. [PubMed: 21301898]
3. Wehrli FW, Saha PK, Gomberg BR, et al. Role of magnetic resonance for assessing structure and function of trabecular bone. Top Magn Reson Imaging. 2002; 13:335–355. [PubMed: 12464746]
4. Watts NB. Fundamentals and pitfalls of bone densitometry using dual-energy X-ray absorptiometry (DXA). Osteoporos Int. 2004; 15:847–854. [PubMed: 15322740]
5. Bolotin HH. DXA in vivo BMD methodology: an erroneous and misleading research and clinical gauge of bone mineral status, bone fragility, and bone remodelling. Bone. 2007; 41:138–154. [PubMed: 17481978]
6. Rizzoli R. Microarchitecture in focus. Osteoporos Int. 2010; 21(Suppl 2):S403–S406. [PubMed: 20464373]
7. Walker MD, Liu XS, Stein E, et al. Differences in bone microarchitecture between postmenopausal Chinese-American and white women. J Bone Miner Res. 2011; 26:1392–1398. [PubMed: 21305606]

8. Liu XS, Walker MD, McMahon DJ, et al. Better skeletal microstructure confers greater mechanical advantages in Chinese–American women versus white women. J Bone Miner Res. 2011; 26:1783–1792. [PubMed: 21351150]
9. Majumdar S. Magnetic resonance imaging of trabecular bone structure. Top Magn Reson Imaging. 2002; 13:323–334. [PubMed: 12464745]
10. Wehrli FW. Structural and functional assessment of trabecular and cortical bone by micro magnetic resonance imaging. J Magn Reson Imaging. 2007; 25:390–409. [PubMed: 17260403]
11. Melton LJ 3rd, Riggs BL, Keaveny TM, et al. Relation of vertebral deformities to bone density, structure, and strength. J Bone Miner Res. 2010; 25:1922–1930. [PubMed: 20533526]
12. Wehrli FW, Gomberg BR, Saha PK, Song HK, Hwang SN, Snyder PJ. Digital topological analysis of in vivo magnetic resonance microimages of trabecular bone reveals structural implications of osteoporosis. J Bone Miner Res. 2001; 16:1520–1531. [PubMed: 11499875]
13. Majumdar S, Link TM, Augat P, et al. Trabecular bone architecture in the distal radius using magnetic resonance imaging in subjects with fractures of the proximal femur. Magnetic Resonance Science Center and Osteoporosis and Arthritis Research Group. Osteoporos Int. 1999; 10:231–239. [PubMed: 10525716]
14. Gold GE, Suh B, Sawyer-Glover A, Beaulieu C. Musculoskeletal MRI at 3.0 T: initial clinical experience. Am J Roentgenol. 2004; 183:1479–1486. [PubMed: 15505324]
15. Robitaille, P-M.; Berliner, LJ. Ultra high-field magnetic resonance imaging. Springer; New York: 2006.
16. Regatte RR, Schweitzer ME. Ultra-high-field MRI of the musculoskeletal system at 7.0T. J Magn Reson Imaging. 2007; 25:262–269. [PubMed: 17260399]
17. Krug R, Stehling C, Kelley DA, Majumdar S, Link TM. Imaging of the musculoskeletal system in vivo using ultra-high field magnetic resonance at 7 T. Invest Radiol. 2009; 44:613–618. [PubMed: 19652609]
18. Krug R, Carballido-Gamio J, Banerjee S, Burghardt AJ, Link TM, Majumdar S. In vivo ultra-high-field magnetic resonance imaging of trabecular bone microarchitecture at 7 T. J Magn Reson Imaging. 2008; 27:854–859. [PubMed: 18383263]
19. Banerjee S, Krug R, Carballido-Gamio J, et al. Rapid in vivo musculoskeletal MR with parallel imaging at 7T. Magn Reson Med. 2008; 59:655–660. [PubMed: 18224700]
20. Chang G, Pakin SK, Schweitzer ME, Saha PK, Regatte RR. Adaptations in trabecular bone microarchitecture in Olympic athletes determined by 7T MRI. J Magn Reson Imaging. 2008; 27:1089–1095. [PubMed: 18425824]
21. Chang G, Friedrich KM, Wang L, et al. MRI of the wrist at 7 tesla using an eight-channel array coil combined with parallel imaging: preliminary results. J Magn Reson Imaging. 2010; 31:740–746. [PubMed: 20187221]
22. Magland JF, Rajapakse CS, Wright AC, Acciavatti R, Wehrli FW. 3D fast spin echo with out-of-slab cancellation: a technique for high-resolution structural imaging of trabecular bone at 7 Tesla. Magn Reson Med. 2010; 63:719–727. [PubMed: 20187181]
23. Bhagat YA, Rajapakse CS, Magland JF, et al. Performance of muMRI-based virtual bone biopsy for structural and mechanical analysis at the distal tibia at 7T field strength. J Magn Reson Imaging. 2011; 33:372–381. [PubMed: 21274979]
24. van Rietbergen B, Majumdar S, Pistoia W, et al. Assessment of cancellous bone mechanical properties from micro-FE models based on micro-CT, pQCT and MR images. Technol Health Care. 1998; 6:413–420. [PubMed: 10100943]
25. Rajapakse CS, Magland J, Zhang XH, et al. Implications of noise and resolution on mechanical properties of trabecular bone estimated by image-based finite-element analysis. J Orthop Res. 2009; 27:1263–1271. [PubMed: 19338030]
26. Finnerty, MYX.; Zheng, T.; Heilman, J.; Castrilla, N.; Herczak, J.; Fujita, H.; Ibrahim, TS.; Boada, F.; Zhao, T.; Schmitt, F.; Stoeckel, B.; Potthast, A.; Wicklow, K.; Trattnig, S.; Mamisch, C.; Recht, M.; Sodickson, D.; Wiggins, G.; Zhu, Y. International Society of Magnetic Resonance in Medicine. Stockholm, Sweden: 2010. A 7-Tesla high density transmit with 28-channel receive-only array knee coil.

27. Krug R, Carballido-Gamio J, Banerjee S, et al. In vivo bone and cartilage MRI using fully-balanced steady-state free-precession at 7 tesla. Magn Reson Med. 2007; 58:1294–1298. [PubMed: 17957777]
28. Kim N, Lee JG, Song Y, Kim HJ, JSY, Cho G. Evaluation of MRI resolution affecting trabecular bone parameters: determination of acceptable resolution. Magn Reson Med. 201110.002/mrm. 22984
29. Vasilic B, Wehrli FW. A novel local thresholding algorithm for trabecular bone volume fraction mapping in the limited spatial resolution regime of in vivo MRI. IEEE Trans Med Imaging. 2005; 24:1574–1585. [PubMed: 16353372]
30. Rajapakse CS, Magland JF, Wald MJ, et al. Computational biomechanics of the distal tibia from high-resolution MR and micro-CT images. Bone. 2010; 47:556–563. [PubMed: 20685323]
31. Wehrli FW, Rajapakse CS, Magland JF, Snyder PJ. Mechanical implications of estrogen supplementation in early postmenopausal women. J Bone Miner Res. 2010; 25:1406–1414. [PubMed: 20200948]
32. Liu XS, Zhang XH, Rajapakse CS, et al. Accuracy of high-resolution in vivo micro magnetic resonance imaging for measurements of microstructural and mechanical properties of human distal tibial bone. J Bone Miner Res. 2010; 25:2039–2050. [PubMed: 20499379]
33. Guo XE, Goldstein XA. Is trabecular bone tissue different from cortical bone tissue? Forma. 1997; 12:185–196.
34. Edwards WT, Zheng Y, Ferrara LA, Yuan HA. Structural features and thickness of the vertebral cortex in the thoraco-lumbar spine. Spine (Phila Pa 1976). 2001; 26:218–225. [PubMed: 11154545]
35. Silva MJ, Wang C, Keaveny TM, Hayes WC. Direct and computed tomography thickness measurements of the human, lumbar vertebral shell and endplate. Bone. 1994; 15:409–414. [PubMed: 7917579]
36. Seeman E. The structural and biomechanical basis of the gain and loss of bone strength in women and men. Endocrinol Metab Clin North Am. 2003; 32:25–38. [PubMed: 12699291]
37. Felson DT, Neogi T. Osteoarthritis: is it a disease of cartilage or of bone? Arthritis Rheum. 2004; 50:341–344. [PubMed: 14872473]
38. De Laet C, Kanis JA, Oden A, et al. Body mass index as a predictor of fracture risk: a meta-analysis. Osteoporos Int. 2005; 16:1330–1338. [PubMed: 15928804]
39. Kanis JA, Johnell O, Oden A, Johansson H, McCloskey E. FRAX and the assessment of fracture probability in men and women from the UK. Osteoporos Int. 2008; 19:385–397. [PubMed: 18292978]
40. Roemer PB, Edelstein WA, Hayes CE, Souza SP, Mueller OM. The NMR phased array. Magn Reson Med. 1990; 16:192–225. [PubMed: 2266841]
41. Wiggins GC, Triantafyllou C, Potthast A, Reykowski A, Nittka M, Wald LL. 32-channel 3 Tesla receive-only phased-array head coil with soccer-ball element geometry. Magn Reson Med. 2006; 56:216–223. [PubMed: 16767762]
42. Wiggins GC, Polimeni JR, Potthast A, Schmitt M, Alagappan V, Wald LL. 96-Channel receive-only head coil for 3 Tesla: design optimization and evaluation. Magn Reson Med. 2009; 62:754–762. [PubMed: 19623621]
43. Krug R, Banerjee S, Han ET, Newitt DC, Link TM, Majumdar S. Feasibility of in vivo structural analysis of high-resolution magnetic resonance images of the proximal femur. Osteoporos Int. 2005; 16:1307–1314. [PubMed: 15999292]

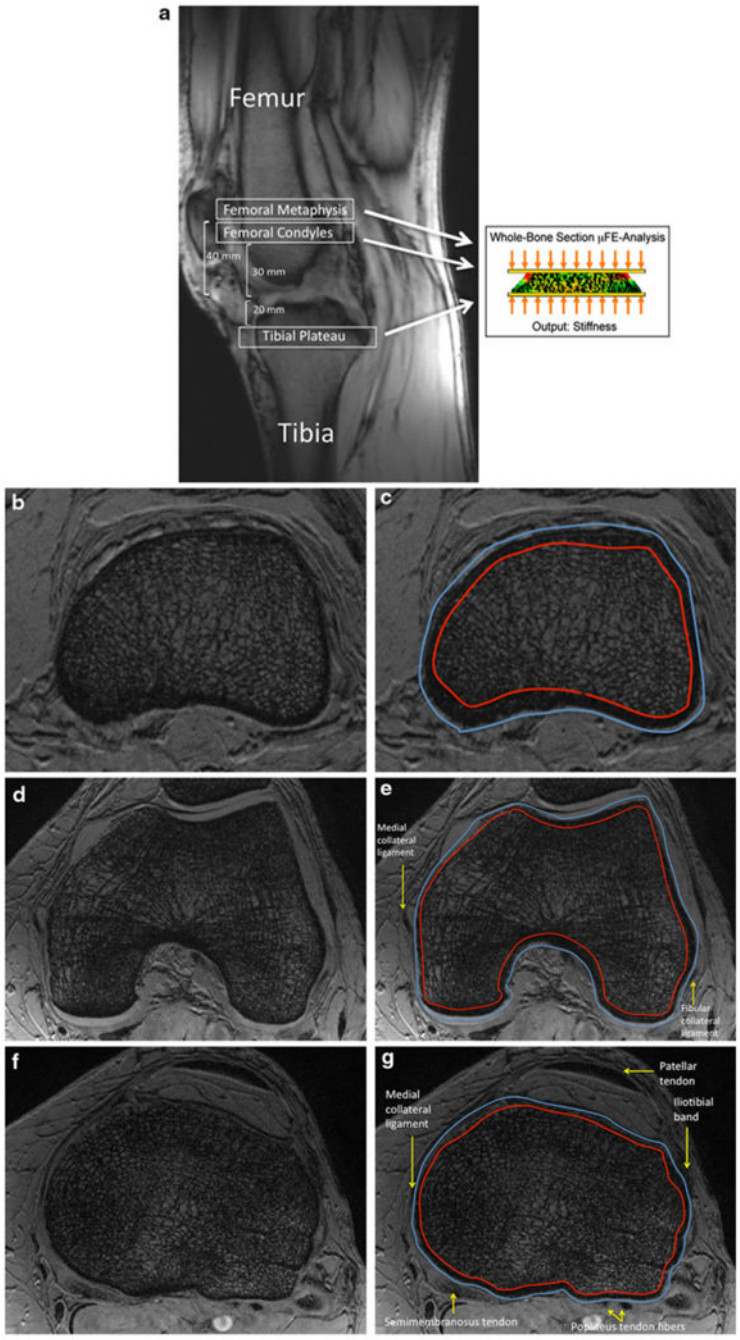

Fig. 1.

a Sagittal MRI localizer image showing the locations of analysis at the distal femoral metaphysis, femoral condyles, and tibial plateau. To compute bone stiffness, μ-FEA was performed using an axial compression simulation. **b** Representative axial 7T MR image at the level of the distal femoral metaphysis with corresponding segmentation shown in (**c**). (In MR images of bone, marrow spaces are *white* and bone is *dark*.) **d** Representative axial 7T MR image at the level of the femoral condyles with corresponding segmentation shown in (**e**). **f** Representative axial 7T MR image at the level of the tibial plateau with corresponding

segmentation shown in (**g**). The *outer* segmentation border indicates the periosteal border of bone. The *inner* segmentation border indicates the endosteal border of bone.

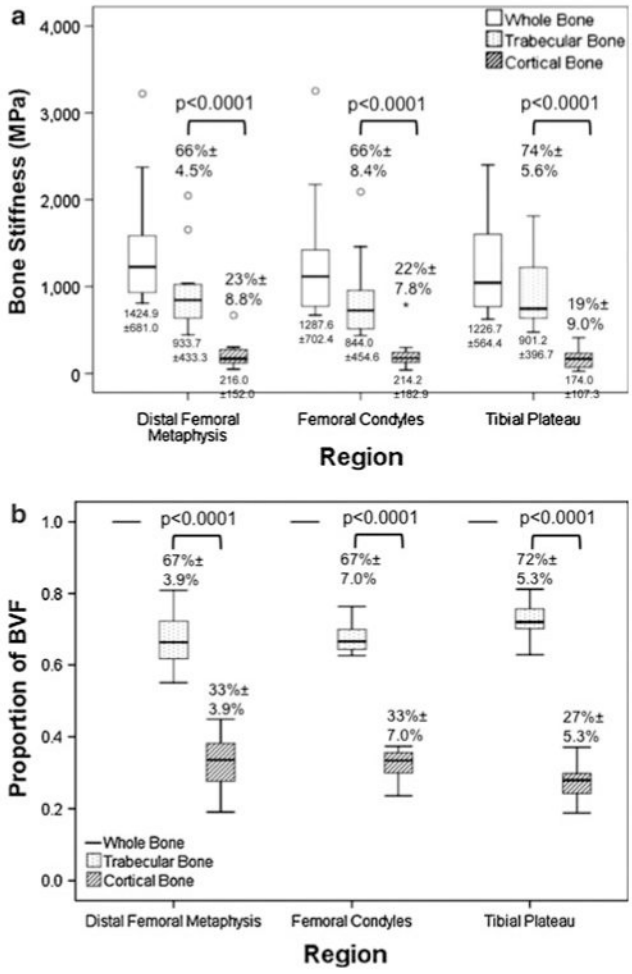

Fig. 2.

a *Boxplots* of data from Table 1 comparing whole, cortical, and trabecular bone stiffness at the distal femoral metaphysis, the femoral condyles, and the tibial plateau. At all locations, trabecular bone stiffness was greater than cortical bone stiffness ($P < 0.0001$). There were no differences in whole, cortical, or trabecular bone stiffness when comparisons were performed between locations ($P > 0.40$). **b** *Boxplots* comparing the proportion of BVF due to trabecular versus cortical bone at the distal femoral metaphysis, the femoral condyles, and the tibial plateau. At all locations, trabecular bone represented a greater proportion of BVF compared to cortical bone ($P < 0.0001$)

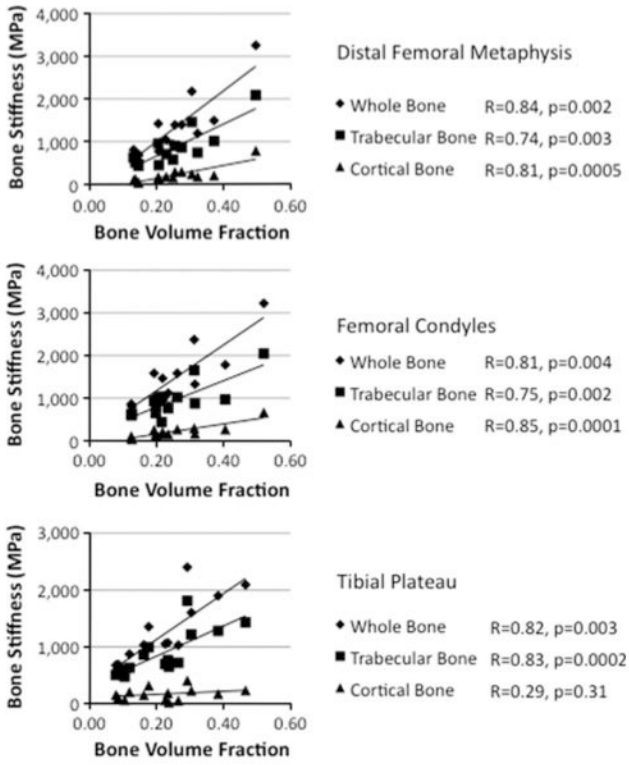

Fig. 3.

Graphs illustrating the relationship between whole, cortical, and trabecular bone stiffness and BVF at the distal femoral metaphysis, femoral condyles, and the tibial plateau. With the exception of cortical bone at the tibial plateau ($R = 0.29$, $P > 0.31$), there was a positive correlation between bone stiffness and BVF ($R = 0.74–0.85$, $P \leq 0.004$ for all)

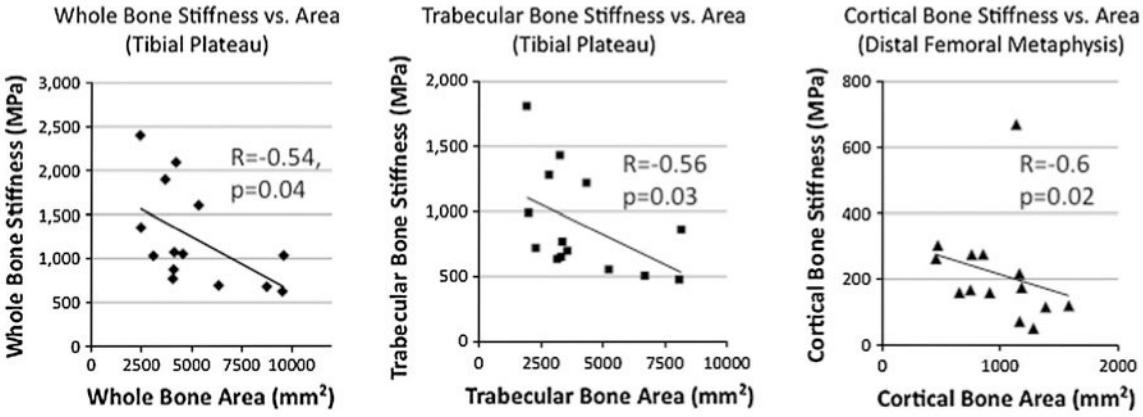

Fig. 4.

Graphs illustrating the negative correlation between whole, trabecular, and cortical bone stiffness and corresponding whole, trabecular, and cortical bone areas at the proximal tibia and distal femoral metaphysis ($R = -0.54$ to -0.6, $P < 0.05$)

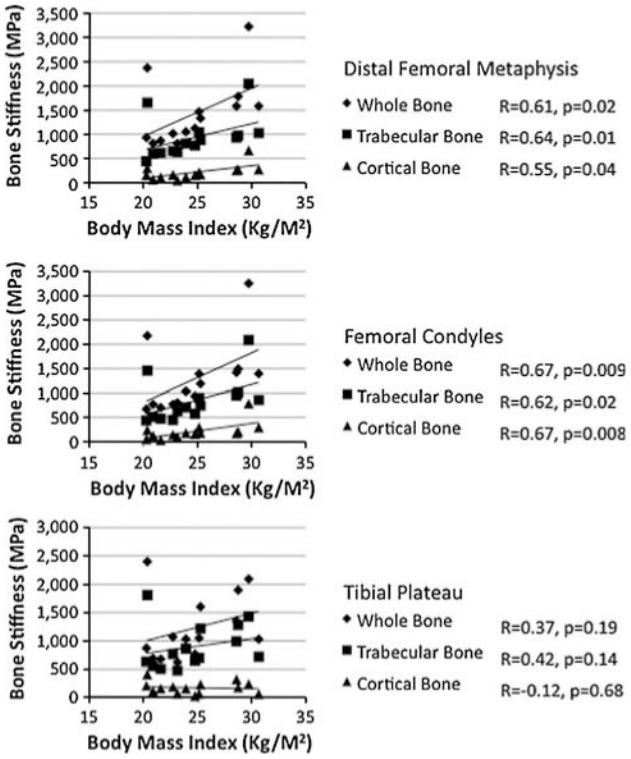

Fig. 5.

Graphs illustrating the relationship between whole, trabecular, and cortical bone stiffness and BMI. Whole, trabecular, and cortical bone stiffness positively correlated with BMI at the distal femoral metaphysis and at the femoral condyles ($R = 0.55-0.67$, $P < 0.05$), but not at the tibial plateau ($R = -0.12$ to 0.42, $P \geq 0.14$)

J Bone Miner Metab. Author manuscript; available in PMC 2013 July 25.

Table 1

Mean values and standard deviations for each MR measurement of bone at each location

MR measure	Distal femoral metaphysis		Femoral condyles		Tibial plateau	
	Mean	SD	Mean	SD	Mean	SD
Whole bone stiffness (MPa)	1424.9	681.0	1287.6	702.4	1226.7	564.4
Cortical bone stiffness (MPa)	216.0	152.0	214.2	182.9	174.0	107.3
Trabecular bone stiffness (MPa)	933.7	433.3	844.0	454.6	901.2	396.7
Whole bone volume fraction	0.25	0.11	0.25	0.1	0.22	0.11
Whole bone area (mm^2)	4120.4	1942.9	5655.9	2346.6	5164.8	2462.4
Cortical bone area (mm^2)	981.8	341.4	1348.9	468.5	1013.7	414.2
Trabecular bone area (mm^2)	3138.6	1626.4	4306.9	1898.1	4151.1	2101.8
Cortical thickness (mm)	4.6	0.71	5.3	0.91	4.1	0.89

Table 2

Reproducibility of bone segmentation was assessed by repeating the image analysis technique three times (each 1 week apart) on five randomly selected subjects

Region	Whole bone		Trabecular bone		Cortical bone	
	Area	Stiffness	Area	Stiffness	Area	Stiffness
Coefficient of variation (%)						
Distal femoral metaphysis	0.7 ± 0.3	0.5 ± 0.1	1.4 ± 0.8	2.1 ± 1.1	1.8 ± 0.6	2.5 ± 0.8
Femoral condyles	0.5 ± 0.2	0.3 ± 0.2	1.1 ± 0.3	1.3 ± 0.3	2.9 ± 1.1	4.9 ± 2.1
Tibial plateau	1.3 ± 0.4	0.4 ± 0.2	1.9 ± 1.1	4.2 ± 5.1	3.0 ± 2.3	3.6 ± 1.8
Intraclass correlation coefficient						
Distal femoral metaphysic	>0.99	>0.99	>0.99	>0.99	>0.99	>0.99
Femoral condyles	>0.99	>0.99	>0.99	>0.99	>0.99	>0.99
Tibial plateau	>0.99	>0.99	>0.99	>0.99	>0.99	>0.99

The reproducibility was assessed using the coefficient of variation (CV) and intraclass correlation coefficient (ICC) on a primary segmentation parameter (cross-sectional area) and on a derived parameter (stiffness)